ISSN 1674-1056
http://cpb.iphy.ac.cn
http://iopscience.iop.org/cpb
中国物理 B
Chinese Physics
中国物理
Chinese Physics B

Oxide-aperture-dependent output characteristics of circularly symmetric VCSEL structure

Wen-Yuan Liao(廖文渊)[1,2], Jian Li(李健)[3], Chuan-Chuan Li(李川川)[2,3], Xiao-Feng Guo(郭小峰)[1], Wen-Tao Guo(郭文涛)[1], Wei-Hua Liu(刘维华)[1,2], Yang-Jie Zhang(张杨杰)[1,2], Xin Wei(韦欣)[2,3], Man-Qing Tan(谭满清)[1,2]
Citation: Chin. Phys. B . 2020, 29(2): 024201 . **doi:** 10.1088/1674-1056/ab5fbd

Journal homepage: http://cpb.iphy.ac.cn; http://iopscience.iop.org/cpb

What follows is a list of articles you may be interested in

High quality 2-μm GaSb-based optically pumped semiconductor disk laser grown by molecular beam epitaxy

Jin-Ming Shang(尚金铭), Jian Feng(冯健), Cheng-Ao Yang(杨成奥), Sheng-Wen Xie(谢圣文), Yi Zhang(张一), Cun-Zhu Tong(佟存柱), Yu Zhang(张宇), Zhi-Chuan Niu(牛智川)
Chin. Phys. B . 2019, 28(3): 034202 . **doi:** 10.1088/1674-1056/28/3/034202

High performance GaSb based digital-grown InGaSb/AlGaAsSb mid-infrared lasers and bars

Sheng-Wen Xie(谢圣文), Yu Zhang(张宇), Cheng-Ao Yang(杨成奥), Shu-Shan Huang(黄书山), Ye Yuan(袁野), Yi Zhang(张一), Jin-Ming Shang(尚金铭), Fu-Hui Shao(邵福会), Ying-Qiang Xu(徐应强), Hai-Qiao Ni(倪海桥), Zhi-Chuan Niu(牛智川)
Chin. Phys. B . 2019, 28(1): 014208 . **doi:** 10.1088/1674-1056/28/1/014208

Room-temperature continuous-wave interband cascade laser emitting at 3.45 μm

Yi Zhang(张一), Fu-Hui Shao(邵福会), Cheng-Ao Yang(杨成奥), Sheng-Wen Xie(谢圣文), Shu-Shan Huang(黄书山), Ye Yuan(袁野), Jin-Ming Shang(尚金铭), Yu Zhang(张宇), Ying-Qiang Xu(徐应强), Hai-Qiao Ni(倪海桥), Zhi-Chuan Niu(牛智川)
Chin. Phys. B . 2018, 27(12): 124207 . **doi:** 10.1088/1674-1056/27/12/124207

Semiconductor photonic crystal laser

Wanhua Zheng(郑婉华)
Chin. Phys. B . 2018, 27(11): 114211 . **doi:** 10.1088/1674-1056/27/11/114211

Electrically pumped metallic and plasmonic nanolasers

Martin T Hill
Chin. Phys. B . 2018, 27(11): 114210 . **doi:** 10.1088/1674-1056/27/11/114210

Oxide-aperture-dependent output characteristics of circularly symmetric VCSEL structure

Wen-Yuan Liao(廖文渊)[1,2], Jian Li(李健)[3], Chuan-Chuan Li(李川川)[2,3], Xiao-Feng Guo(郭小峰)[1], Wen-Tao Guo(郭文涛)[1], Wei-Hua Liu(刘维华)[1,2], Yang-Jie Zhang(张杨杰)[1,2], Xin Wei(韦欣)[2,3], and Man-Qing Tan(谭满清)[1,2,†]

[1] *State Key Laboratory of Integrated Optoelectronic, Institute of Semiconductors, Chinese Academy of Sciences, Beijing* 100083, *China*
[2] *College of Materials Science and Opto-Electronic Technology, University of Chinese Academy of Sciences, Beijing* 100049, *China*
[3] *Laboratory of Nano-photoelectronics, Institute of Semiconductors, Chinese Academy of Sciences, Beijing* 100083, *China*

(Received 12 September 2019; revised manuscript received 23 October 2019; accepted manuscript online 9 December 2019)

The influence of oxidation aperture on the output characteristics of the circularly symmetric vertical-cavity-surface-emitting laser (VCSEL) structure is investigated. To do so, VCSELs with different oxide aperture sizes are simulated by the finite-difference time-domain (FDTD) method. The relationships among the field distribution of mode superposition, mode wavelength, output spectra, and far-field divergence with different oxide apertures are obtained. Further, VCSELs respectively with oxide aperture sizes of 2.7 μm, 4.4 μm, 5.9 μm, 7 μm, 8 μm, 9 μm, and 18.7 μm are fabricated and characterized. The maximum output power increases from 2.4 mW to 5.7 mW with oxide aperture increasing from 5.9 μm to 9 μm. Meanwhile, the wavelength tuning rate decreases from 0.93 nm/mA to 0.375 nm/mA when the oxide aperture increases from 2.7 μm to 9 μm. The thermal resistance decreases from 2.815 °C/mW to 1.015 °C/mW when the oxide aperture increases from 4.4 μm to 18.7 μm. It is demonstrated theoretically and experimentally that the wavelength spacing between adjacent modes increases with the augment of the injection current and the spacing becomes smaller with the oxide aperture increasing. Thus it can be reported that the aperture size can effectively reduce the mode overlaying but at the cost of the power decreasing and the wavelength tuning rate and thermal resistance increasing.

Keywords: finite-difference time-domain (FDTD), vertical-cavity-surface-emitting laser (VCSEL), oxide aperture, wavelength spacing

PACS: 42.55.PX **DOI:** 10.1088/1674-1056/ab5fbd

1. Introduction

Vertical-cavity surface-emitting laser (VCSEL) is proved to be a powerful competitor to edge-emitting semiconductor laser because of its significant advantages such as low threshold current, circular output beam, high-speed modulation, low cost, and easy fabrication in two-dimensional (2D) arrays.[1–3] These advantages enabled it to be extensively applied to high-power laser source, short-distance optical interconnection, chip-scale atomic clocks, and photonic neuromorphic computing.[4–14] In addition, the full width half maximum (FWHM) of VCSEL's emission spectrum is usually less than 1 nm and its temperature dependence is shifted at a rate of 0.065 nm/°C, which is smaller than edge emitter's or LED's (about 0.3 nm/°C). This allows the narrow band filter to be used to remove the unwanted background and improve the signal-to-noise ratio (SNR), which is very attractive for many applications. Nowadays, VCSELs emitting at various wavelengths are widely studied and some of them, such as 980 nm, 850 nm, and 780 nm devices, even are commercialized.[15–18]

VCSEL with an operating wavelength of 850 nm has aroused the great interest in short-haul optical communication. Due to optical and electric confinement of the oxidation layer, VCSEL devices can achieve only a low threshold single-mode laser output. In order to improve VCSEL's output performance, one has studied the influence of the oxidation layer on output characteristics of VCSELs. In 2002, Hawkins *et al.* analyzed the effect of oxidation aperture size on VCSEL's reliability. It proved that the device with a larger aperture size has higher reliability.[19] Chang *et al.* utilized multiple oxidation layers to reduce the parasitic effect of VCSELs in 2006, and in this way high efficiency and modulation rate devices were implemented.[20] In 2009, the electro–optical characteristics of VCSELs fabricated on the same 850-nm epitaxial wafer with various oxide aperture sizes were presented by Sharizal *et al.*, which revealed high efficiencies of the fabricated VCSEL devices.[21] Choi *et al.*[22] studied the thermal property of the 850-nm devices by using thermal–electric direct-coupled field analysis. It is found that the smaller the oxidation aperture, the greater the thermal resistance of the device will be.

In this paper, the output characteristics of the 850-nm VCSELs with various oxide apertures are presented. First, the relationship among the electric field distribution, output wavelength, output spectra, and far-field divergence with different oxide apertures are calculated by the FDTD solution. Then, the electro–optical characteristics, output spectral, and near-field characteristics for some devices are measured. Also, the relationship between the wavelength spacing with oxide aperture and current is illustrated in both theory and experiment.

†Corresponding author. E-mail: mqtan@semi.ac.cn

© 2020 Chinese Physical Society and IOP Publishing Ltd

The results indicate that the oxide aperture size has a great effect on the output characteristics of VCSELs.

2. Mode calculation and analysis

The FDTD method, in which difference instead of differential is used, is suitable to analyzing the electromagnetic fields of any complex structures. The FDTD simulation results of the VCSEL structure, optical field, and refractive index distribution are shown in Fig. 1. In Fig. 2, the three-dimensional (3D) electric field distributions of mode superposition with numerous oxidation apertures are obtained. It can be seen that the VCSEL realizes the fundamental transverse mode output when the oxidation aperture is 2 μm. With the aperture size increasing, the high-order mode appears, the distribution of the electric field becomes more complex and the area of the electric field increases.

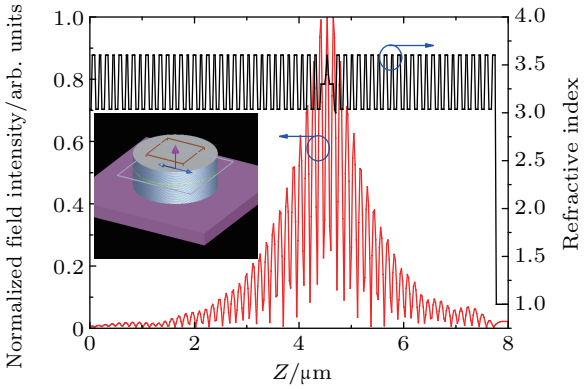


Fig. 1. Standing-wave pattern of optical field and refractive index distribution in VCSELs. Inset: FDTD simulation model of VCSEL on perspective view.

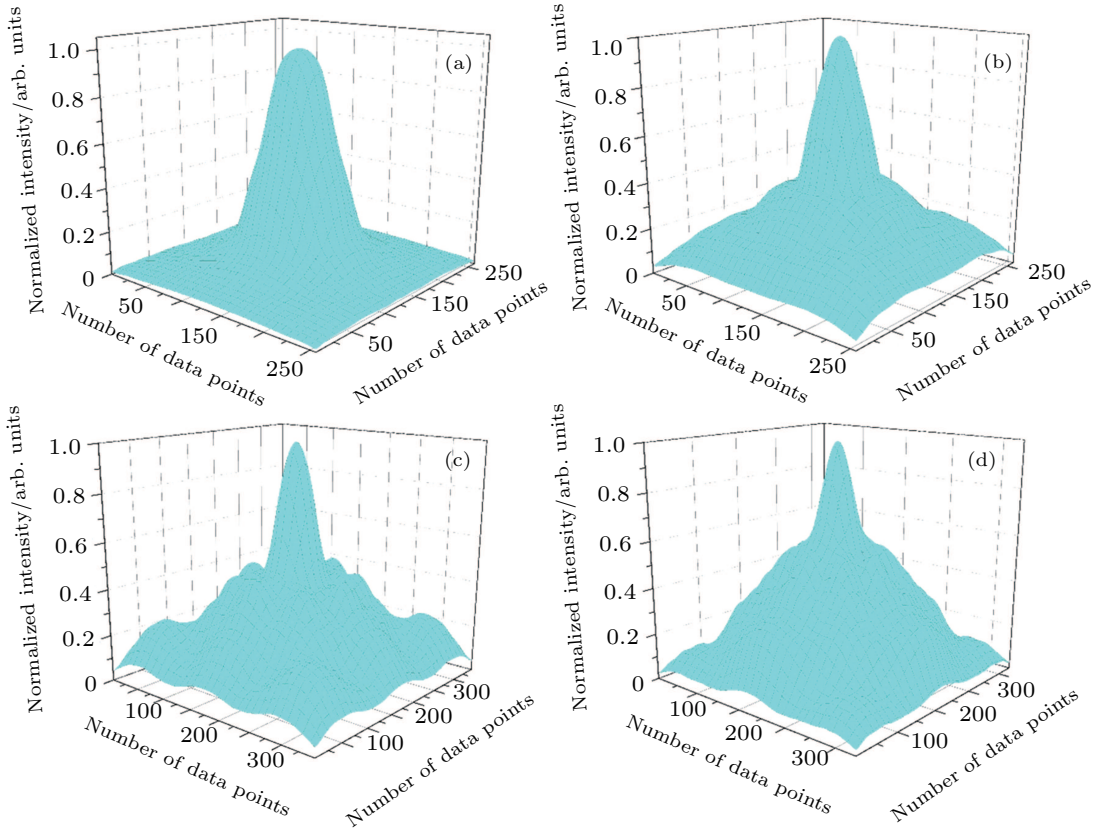


Fig. 2. The 3D electric field distributions of mode superposition with oxidation aperture of (a) 2 μm, (b) 3 μm, (c) 6 μm, and (d) 9 μm.

Figure 3 shows the wavelength of modes and the model order in VCSELs with different oxidation aperture sizes. As can be seen from the figure, when the oxidation aperture is 2 μm, the wavelength of the fundamental transverse mode LP_{01} is 0.8466 μm, while the oxidation aperture increases to 9 μm, LP_{01} wavelength is 0.8484 μm, and wavelength shifts 1.8 nm. That is, with the augment of oxidation aperture, the corresponding wavelength of each mode will increase. The inset of Fig. 3 shows the radiation intensity distributions of several low order transverse modes. It can be found that the peak power of the fundamental mode is located in the center, while the peak power of the higher-order mode is closer to the edge. The distribution expansion of transverse modes indicates that the higher-order mode appears with oxide aperture increasing. In addition, for the standard circular symmetric VCSEL structure, the wavelength λ_{lp} can be expressed as

$$\lambda_{lp} = \lambda_0[1-(2p+l-1)\cdot\lambda_0\sqrt{n_c^2-n_s^2}/2\pi a n_c^2], \qquad (1)$$

where λ_{lp} is the wavelength corresponding to each lp mode; λ_0 is the central wavelength; a is the oxidation aperture radius;

n_c is the core index of refraction; n_s is the cladding index of refraction. It shows that the modes with the same mode index $m = 2p + l - 1$ have the same emission wavelength. From Eq. (1), the mode spacing between adjacent modes is

$$\Delta\lambda = \lambda_0^2 \sqrt{n_c^2 - n_a^2}/2\pi a n_c^2. \tag{2}$$

Equation (2) indicates that the wavelength spacing is related only to the central wavelength, oxidation aperture and effective refractive index. In other words, each mode wavelength spacing is equal in the standard circular symmetry structure with the same oxidation aperture.

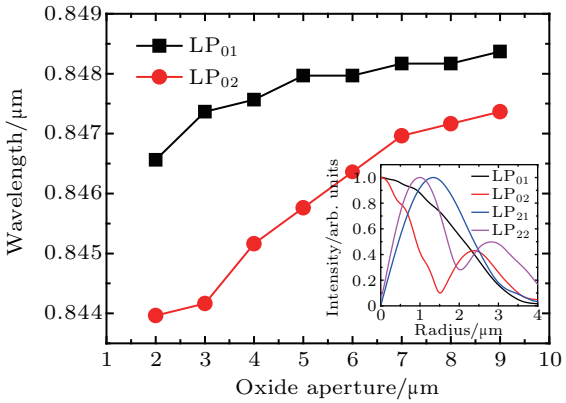


Fig. 3. Wavelength for the LP_{01} and LP_{02} modes *versus* aperture diameter for the VCSEL. Inset: radial intensity distributions of several lower transverse modes in 6-μm oxide aperture VCSEL.

The number of guide modes is determined by the normalized frequency V

$$V = \frac{2\pi a}{\lambda}\sqrt{n_c^2 - n_s^2}. \tag{3}$$

Waveguide is of single mode if $V < 2.405$;[23] for a large V, the number of the guided transverse modes can be estimated from

$$M = \frac{V^2}{4}. \tag{4}$$

The normalized mode intensity is given by[24]

$$I(r,\theta) = \frac{4}{\ell!}\frac{1}{w^2}\left(\frac{2r^2}{w^2}\right)^{\ell}\exp\left(\frac{-2r^2}{w^2}\right)\frac{1}{\pi}\cos^2(\ell\theta), \tag{5}$$

where ℓ is azimuthal index, r and θ are the radial and azimuthal coordinate, respectively. The waist parameter is given by $w^{-2} = k_0 a/2$.

It is further known from Fig. 4(a) that the number of lasing modes increases and the distance between adjacent modes decreases with oxidation aperture increasing. This is because the confinement effect of the transverse mode reduces and the anisotropy of the spatial distribution gradually decreases as the oxidation aperture enlarges. As a result, the increasing of oxidation aperture makes the wavelength of each mode closer to the central wavelength, and reduces the spatial distance between adjacent modes. Figure 4(b) shows that the far-field divergence angle of the fundamental mode decreases with oxidation aperture increasing. When the oxidation aperture increases from 3 μm to 9 μm, the FWHM of the angle decreases from 12.8° to 6.2°.

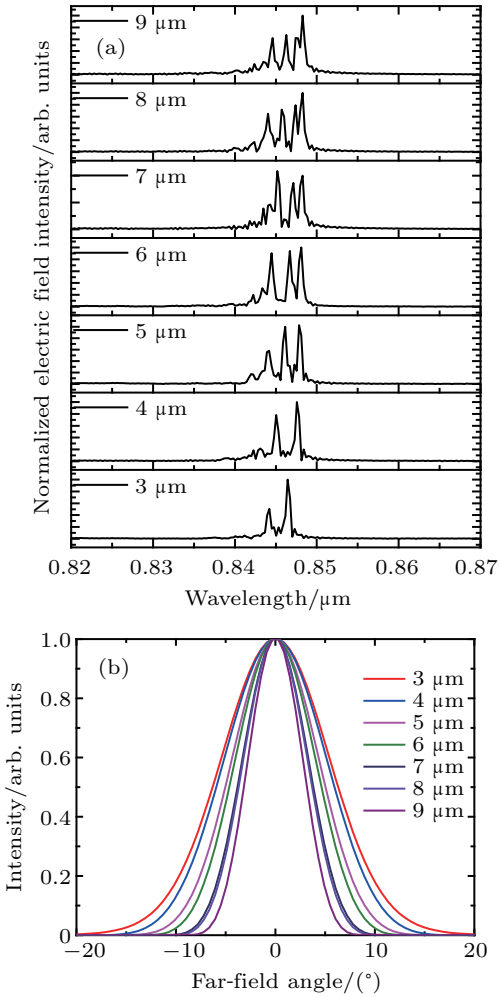


Fig. 4. (a) Spectra and (b) imtensities *versus* far-field divergence angle at different oxidation apertures.

3. Device structure and fabrication

A single 850-nm VCSEL structure is shown schematically in Fig. 5(a). The epitaxial wafer used in this study is grown on an N-type GaAs substrate by metal–organic chemical vapor deposition. The N-DBR is composed of 35 pairs of $Al_{0.12}Ga_{0.88}As/Al_{0.9}Ga_{0.1}As$, and the P-DBR is comprised of 23 pairs of $Al_{0.12}Ga_{0.88}As/Al_{0.9}Ga_{0.1}As$. The active region with three GaAs quantum wells is separated by an undoped $Al_{0.3}Ga_{0.7}As$ separate confinement heterostucture layer, which is sandwiched between N-DBR and P-DBR. A high-aluminum content layer is placed near the first pair of the P-DBR to form the oxide aperture. The topmost DBR layer is a highly p^+-doped GaAs layer with a thickness of 50 nm, which is on the top of the p-type DBR as a low contact resistance layer.

The fabrication begins to form a mesa structure which isolates various VCSEL devices and exposes the high-aluminum-content oxidation layer. The technique includes the deposition of the SiO_2 layer due to the plasma-enhanced chemical vapor deposition. Such a dielectric layer is then patterned by using standard optical lithography and wet chemical etching. This patterned dielectric serves as a mask for the mesas which are etched by inductively couple plasma. The high-aluminum-content layer is then selectively oxidized by wet oxidation to form an aperture. The exposed $Al_{0.98}Ga_{0.02}As$ layer is oxidized at 420 °C in N_2/H_2O atmosphere. Dry N_2 with a constant flow rate of 1.2 L/min is used as carrier gas for the H_2O vapor. The water temperature is maintained at 95 °C. The oxidation time is maintained for 18 min. The cross-section of the oxided sample is observed by SEM and the oxidation depth of sample is measured as shown in Fig. 5(b). After that, an electrode ring contact pattern is formed by secondary photolithography and a light aperture pattern is produced by third lithography. In order to form a p-type ohmic contact, Ti–Pt–Au layers are evaporated, and then lifted off. On the back side, the substrate is thinned to less than 150-μm thick, followed by Au–Ge–Ni evaporation to form N-type electrode.

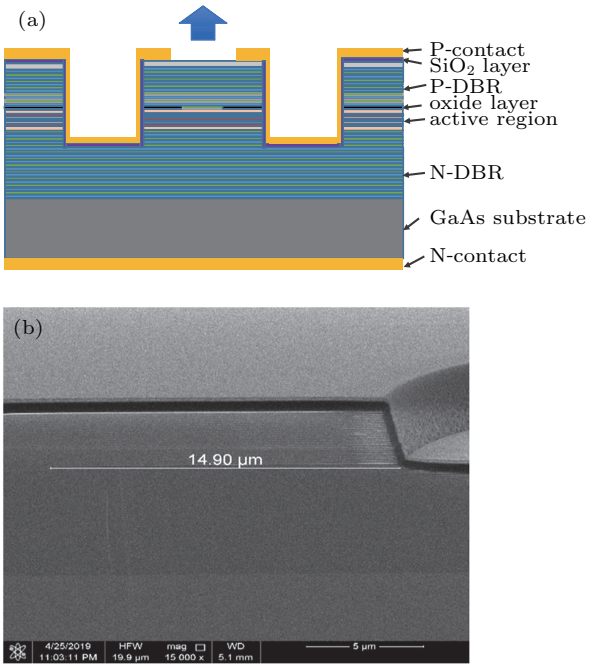


Fig. 5. (a) Schematic diagram of 850-nm VCSEL device, and (b) SEM image of device's cross section.

4. Experimental results and discussion

Variations of power and voltage with current are shown in Fig. 6, indicating the light–current (*L–I*) characteristics of VCSELs with oxide apertures of 5.9 μm, 7 μm, 8 μm, and 9 μm, and the corresponding mesa sizes of 36 μm, 37 μm, 38 μm, and 39 μm, respectively. The aperture sizes are measured by an infrared light source CCD system as shown in the inset. The maximum output power increases from 2.4 mW to 5.7 mW and the power saturation current shifts from 7 mA to 12 mA with oxide aperture increasing from 5.9 μm to 9 μm. The *V–I* characteristics of the fabricated VCSELs for different oxide apertures are shown in Fig. 6(b). As can be seen, the slope of the *V–I* curve decreases with oxide aperture increasing, thereby reducing the differential series resistance.

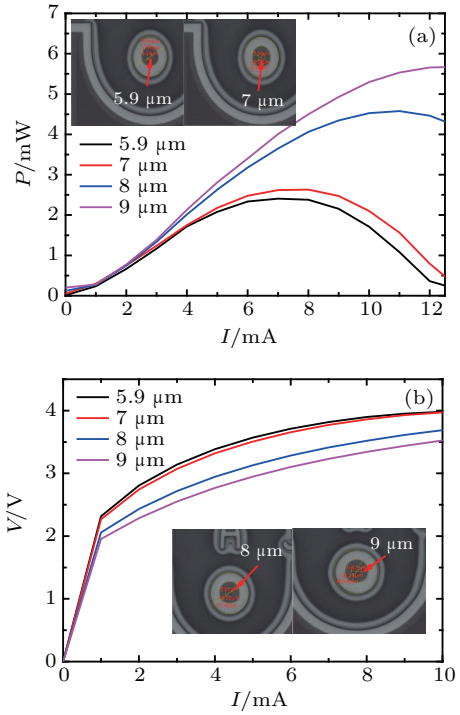


Fig. 6. The *L–I* and *V–I* characteristics of fabricated VCSEL devices with various oxide apertures. Insets show top view of oxidation aperture at (a) 5.9 μm, 7 μm and (b) 8 μm, 9 μm, respectively.

Figures 7(a) and 7(b) show the electro–optical characteristics of VCSELs with 2.7 μm and 4.4 μm, and the corresponding mesa sizes are 33 μm, 34 μm, respectively. Figure 7(c) shows the variation of device resistance with oxidation aperture size. We observe that the resistance decreases with increasing sizes of VCSEL aperture. Figure 7(d) shows the spectral characteristics of VCSELs with 2.7-μm, 4.4-μm, and 9-μm oxide apertures, which are measured under the continuous-wave condition at room temperature. A redshift of the central wavelength is observed with increasing current due to thermal effects. In the current range between 1 mA and 8 mA, the wavelength shift of the 2.7-μm device is 7.46 nm, corresponding to a tuning rate of 0.93 nm/mA. For a larger device with 9-μm oxide aperture, the wavelength shift is only 3.0 nm with a tuning rate of 0.375 nm/mA.

Figure 8 depicts the spectra of VCSELs with different aperture sizes and currents. Figure 8(a) shows thespectra of 2.7 μm, 4.4 μm, and 9 μm at 2 mA. It can be seen from the figure that the mode orders are both 2, the wavelengths of the first mode LP_{01} are 847.1 nm, 847.88 nm, and 846.54 nm, while the wavelengths of the second mode LP_{11} are 846.18 nm, 847.28 nm, and 845.88 nm, respectively. The wavelength spacing between two modes of 2.7-μm, 4.4-μm, and 9-μm

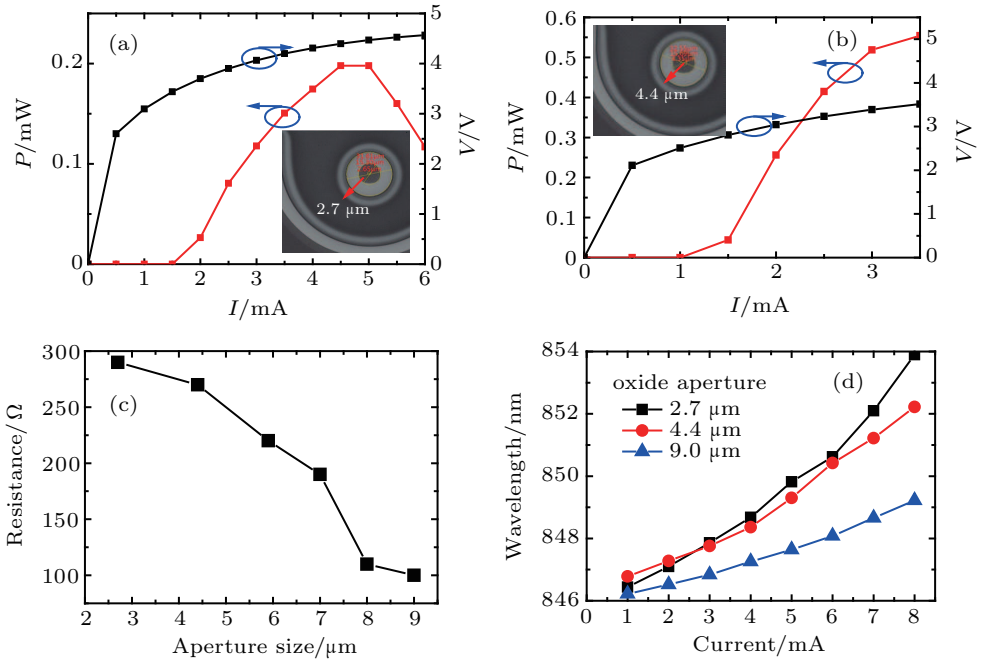


Fig. 7. (a) *L–I–V* characteristic of 2.7-μm device, (b) *L–I–V* characteristic of 4.4-μm device, (c) variation of resistance with aperture size, and (d) plots of wavelength *versus* current of devices with different oxide apertures at room temperature.

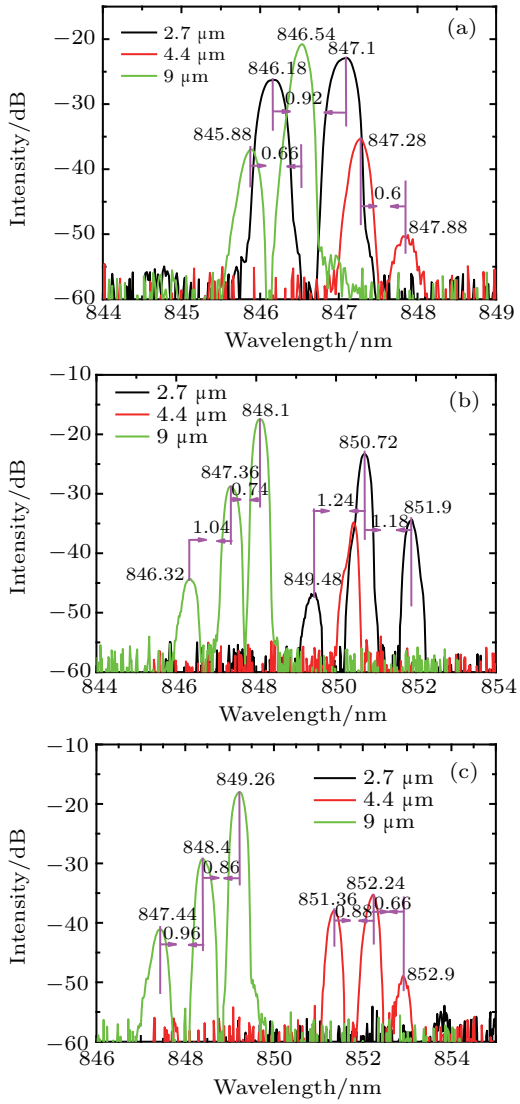


Fig. 8. Spectra of VCSELs with different aperture sizes at (a) $I = 2$ mA, (b) $I = 6$ mA, and (c) $I = 8$ mA.

VCSELs decreases from 0.92 nm to 0.66 nm. Figures 8(b) and 8(c) show the spectra of these VCSELs at 6-mA and 8-mA bias currents, respectively. The mode order increases to 3, and another mode LP_{21} appears. For a 2.7-μm device, the wavelength spacing between adjacent modes is 0.92 nm at 2 mA and 1.18 nm at 6 mA. For a 9-μm device, the wavelength spacing is 0.66 nm, 0.74 nm, and 0.86 nm corresponding to the current of 2 mA, 6 mA, and 8 mA, respectively. It indicates that the wavelength spacing increases with current increasing. According to Ref. [25], we can obtain

$$\Delta n = -\left(\frac{e^2\lambda^2}{8\pi^2 c^2 \varepsilon_0 n}\right)\left(\frac{N}{m_e} + \frac{P}{m_h}\right), \tag{6}$$

where λ is the photon wavelength, e is the electron charge, ε_0 is the permittivity of free space, m_e and m_h are the effective mass of electron and hole, electron and hole concentration are N and P, respectively. The relationship between current density and carrier concentration is

$$J = q(v_e N + v_h P), \tag{7}$$

where v_e and v_h are the drift velocity of electron and hole. According to Eq. (7), the carrier density increases with the current increasing, resulting in refractive index decreasing (see Eq. (6)). Finally the emitting wavelength spacing also increases (Eq. (2)). It can be seen from the figures that the wavelength spacing becomes smaller with oxide aperture increasing. It is consistent with Eq. (2).

Figure 9 shows the spectra and near-field images of the 9-μm VCSEL at different currents. It indicates that the output mode of the device increases with the augment of the injection current, which is consistent with the theory.

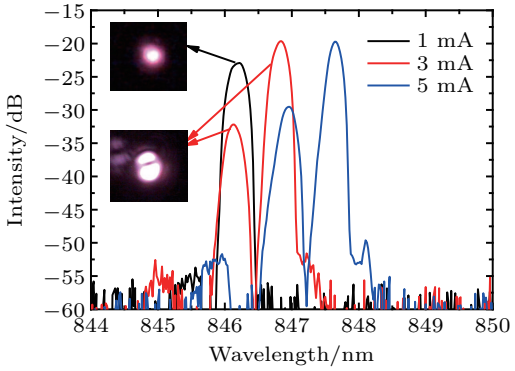


Fig. 9. Spectra and near-field images of 9-μm VCSEL.

The plots of central wavelength *versus* dissipated power for different oxide apertures are shown in Fig. 10. As seen in Fig. 10, wavelength shifts linearly with dissipated power increasing. Because thermal resistance is defined as

$$R_{\mathrm{th}} = \frac{\Delta T}{\Delta P_{\mathrm{heat}}} = \frac{\Delta\lambda/\Delta P_{\mathrm{heat}}}{\Delta\lambda/\Delta T} = \frac{C_1}{C_2}, \tag{8}$$

where the parameters C_1 and C_2 are the wavelength shifts with the increase of dissipated power and ambient temperature, respectively, the dissipated power P_{heat} is defined as

$$P_{\mathrm{heat}} = P_{\mathrm{el}} - P_{\mathrm{opt}} = IV - P_{\mathrm{opt}}, \tag{9}$$

with the electrical power being $P_{\mathrm{el}} = IV$ and the optical output power being P_{opt}. For VCSELs with an emission wavelength in a range of 800 nm–1000 nm, a mode shift of $\Delta\lambda/\Delta T$ is 0.065 nm/°C. Therefore, the thermal resistance can be precisely obtained from the slope of the linear fit to the data points by using least square fit. For 4.4-μm, 8-μm, 9-μm, and 18.7-μm devices, the slope is 0.183 nm/mW, 0.168 nm/mW, 0.155 nm/mW, and 0.066 nm/mW corresponding to the thermal resistances of 2.815 °C/mW, 2.585 °C/mW, 2.385 °C/mW, and 1.015 °C/mW, respectively. It is found that the thermal resistance decreases significantly with the increase of oxide aperture. This corresponds to the longitudinal heat flow from a uniform-temperature circular area, whose size is equal to the diameter of the oxidation aperture, to a substrate of the same

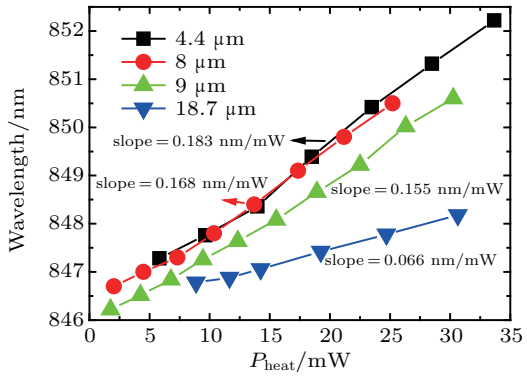


Fig. 10. Plots of wavelength shift *versus* dissipated power for VCSELs with different oxide apertures.

thermal conductivity. It can be known that the smaller the oxidation aperture size, the smaller the heat flux is. At the same time, due to the same distance from the different oxidation apertures to the side wall of the mesa, the lateral heat flow from the active region to the side wall of the mesa is identical for different oxidation aperture sizes. Therefore,thermal resistance is inversely proportional to the size of the oxide aperture.

5. Conclusions

In this work, we theoretically demonstrate the electric field distribution of mode superposition, the wavelength of mode, and the wavelength spacing between adjacent modes in VCSELs with several oxidation apertures. We find that the corresponding wavelength of each mode increases with the augment of oxidation aperture. When the oxidation aperture increases from 3 μm to 9 μm, the distance between adjacent modes decreases and the far-field divergence angle of the fundamental mode decreases from 12.8° to 6.2°. Spectra, wavelength drifts and thermal resistances of devices with different oxide apertures are measured. The wavelength drift rate decreases from 0.93 nm/mA to 0.375 nm/mA when the oxide aperture increases from 2.7 μm to 9 μm and the thermal resistance increases significantly with oxide aperture size decreasing. In addition, We find that the wavelength spacing increases with the augment of the injection current, and it also becomes smaller with oxide aperture increasing, which are consistent with the theoretical results. Through the studies of the spectrum mode characteristics, these modes can be locked to form a mode-locked laser and applied to precision measurements. In this work, the effects of the oxidation aperture and the injection current on output characteristics of the 850 nm circularly symmetric VCSEL structure are comprehensively analyzed.

References

[1] Iga K 2000 *IEEE J. Sel. Top. Quantum Electron.* **6** 1201
[2] Koyama F 2006 *IEEE J. Lightw. Technol.* **24** 4502
[3] Zhao Z B, Xu C, Xie Y Y, Zhou K, Liu F and Shen G D 2012 *Chin. Phys. B* **21** 034206
[4] Seurin J F, Zhou D L, Xu G Y, *et al.* 2016 *Proc. SPIE* **9766** 97660D
[5] Zhou D L, Seurin J F, Xu G Y, *et al.* 2014 *Proc. SPIE* **9001** 90010E
[6] Seurin J F, Xu G Y, Wang Q, *et al.* 2010 *Proc. SPIE* **7615** 76150F-1
[7] Kasukawa A, Takaki K, Imai S, Shimizu H, *et al.* 2011 *Proc. IEEE Photon. Conf.* **393**
[8] Jackson K P and Schow C L 2013 *VCSEL-Based Transceivers for Data Communications* (Berlin: Springer), pp. 431–448
[9] Westbergh P, Safaisini R, Haglund E, *et al.* 2012 *Electron. Lett. Vol* **48** 1145
[10] Kuchta D M, Schow C L, Baks C W, Westbergh P, Gustavsson J S and Larsson A 2015 *IEEE Photon. Technol. Lett.* **27** 577
[11] Xiang L, Zhang X, Zhang J W, Ning Y Q, Werner Hofmann and Wang L J 2017 *Chin. Phys. B* **26** 074299
[12] Robertson J, Wade E and Hurtado A 2019 *IEEE J. Selec Top. Quantum Electron.* **25** 5100307

[13] Xiang S Y, Zhang Y H, Gong J K, *et al.* 2019 *IEEE J. Selec Top. Quantum Electron.* **25** 1700109
[14] Xiang S Y, Zhang Y H, Guo X X, Wen A J and Hao Y 2018 *J. Lightwave Technol.* **36** 4227
[15] Sakaguchi J, Katayama T and Kawaguchi H 2010 *Opt. Express* **18** 12362
[16] Kuo Y K, Chen J R, Chen M L and Liou B T 2007 *Appl. Phys. B* **86** 623
[17] Iga K 2008 *Jpn. J. Appl. Phys.* **47** 1
[18] Iga K 2018 *Jpn. J. Appl. Phys.* **57** 08PA01
[19] Hawkins B M, Hawthorne R A, Guenter J K, *et al.* 2002 *Electronic Components and Technology Conference*, May 28–31, 2002, San Diego, USA, p. 540
[20] Chang Y C, Wang C S, Johansson L A, *et al.* 2006 *Electron. Lett.* **42** 1281
[21] Sharizal A M, Leisher P O, Choquette K D, *et al.* 2009 *Optik* **120** 121
[22] Choi J H, Wang L, Bi H and Chen R T 2006 *IEEE J. Sel. Top. Quantum Electron.* **12** 1060
[23] Saleh B E A and Teich M C 2007 *Fundamentals of Photonics* (New York: John Wiley & Sons) p. 331
[24] Pereira S, Willemsen M, Exter M V and Woerdman J 1998 *Appl. Phys. Lett.* **73** 2239
[25] Henry C H, Logan R A and Bertness K A 1981 *J. Appl. Phys.* **52** 4457